Journal of The Electrochemical Society

OPEN ACCESS

Impedance Spectroscopy Characterization of PEM Fuel Cells with Fe-N-C-Based Cathodes

Impedance Spectroscopy Characterization of PEM Fuel Cells with Fe-N-C-Based Cathodes

Tatyana Reshetenko,[1,*] Alexey Serov,[2,*] Andrei Kulikovsky,[3,*,z] and Plamen Atanassov[4,*]

[1]*Hawaii Natural Energy Institute, University of Hawaii, Honolulu, Hawaii 96822, USA*
[2]*Pajarito Powder, LLC, Albuquerque, New Mexico 87109-4427, USA*
[3]*Forschungszentrum Jülich GmbH, Institute of Energy and Climate Research, IEK-3: Electrochemical Process Engineering, D-52425 Jülich, Germany*
[4]*Chemical & Biomolecular Engineering Department, National Fuel Cell Research Center, University of California, Irvine, California 92697-2580, USA*

We report impedance spectroscopy analysis of PEM fuel cells built with platinum group metal-free (PGM-free) Fe-N-C cathodes with the catalyst loading and ionomer to catalyst ratio being variable parameters. The dependence of key cathode transport and kinetic parameters on the cell current density J are obtained in the range from 0.025 to 0.4 A cm^{-2}. The electrode performance is evaluated using the characteristic current densities for proton and oxygen transport in the cathode catalyst layer. Overall, certain electrode configurations demonstrate proton and oxygen transport properties comparable to those of Pt/C systems, making them promising substitutes for platinum at cathodic side of PEM fuel cells.
 [DOI: 10.1149/2.1431910jes]

Manuscript submitted April 11, 2019; revised manuscript received June 3, 2019. Published June 26, 2019.

Christian Friedrich Schoenbein discovered fuel cell effect in a simple experiment with two platinum wires immersed in electrolyte solution.[1] Ever since, due to its unique properties for oxygen reduction, platinum has been a material of choice for low-temperature fuel cell electrodes. However, having a high price volatility between 25 and 50 USD per gram and limited supply resources, Pt is insecure material for mass integration of fuel cell systems onto the market. Modern best-performing electrodes utilize up to 0.4 mg$_{Pt}$ cm^{-2} on either side of the cell. With the cell power density on the order of 1 W cm^{-2} at operational voltage, this translates into 80 g of Pt for a 100kW stack (based on net power output). Clearly, a less expensive alternative is utterly desirable.

In the past decade, a lot of efforts have been done to develop a platinum group metal-free (PGM-free), cathodic materials for proton exchange membrane fuel cells (PEMFCs) (we refer reader to recent reviews).[2,3] At present, Fe-N-C systems are considered as one of the most promising alternatives to classic Pt/C cathodes. Recently, a PEM fuel cell equipped with the Fe-N-C cathode exhibiting peak power density of about 0.5 W cm^{-2} has been demonstrated.[4] The importance of substitution of platinum with PGM-free ORR catalysts resulted in establishing in USA ElectroCat consortium under the U.S. Department of Energy's Clean Energy Manufacturing Initiative.[2]

One of the key problems in M-N-C (where M = Fe, Co, Ni, Mn) electrodes is understanding the oxygen reduction reaction (ORR) mechanism. A combination of micro-structural, spectroscopic, and electrochemical studies indicated that the ORR in some of these systems proceeds through formation of hydrogen peroxide (2 e$^-$), while the contribution of a direct four-electron oxygen reduction to water is seemingly small.[5,6] Moreover, the balance between 2- and 4-electron pathways depends on the cell current density J, which translates into strong variation of the ORR Tafel slope with current.[7] Previously it was shown that polarization curves exhibit transition from low to high Tafel slope starting at the electrode currents as low as 0.01 A cm^{-2}.[8] In addition, according to previously published data,[7] the exchange current density for the 2-electron peroxide formation reaction is several orders of magnitude larger than this parameter for the direct oxygen reduction to water. More uncertainty in reaction kinetics add multiple structures of potential Fe-N-C sites.[9–11]

A standard approaches of electrocatalysts characterization are based on analysis of voltammograms obtained in rotating ring disk electrode (RRDE) and/or polarization curves measured in fuel cell experiments.[5,8,12] The RRDE experiments give details of the ORR kinetics, while the cell polarization curves yield merely the ORR Tafel slope. Determination of proton conductivity and oxygen mass transport coefficients in application-relevant electrodes requires another technique.

Much less work has been done on impedance spectroscopy characterization of PGM-free systems. Malko et al. used electrochemical impedance spectroscopy (EIS) to determine an optimal ionomer to carbon ratio for the M-N-C (M = Fe, Co, Ni, Mn etc.) cathodes.[13] They specifically analyzed the high-frequency part of impedance spectra which exhibits the rate of proton transport in the porous electrodes; however, the oxygen mass transport effects were beyond the mentioned above study. Herein, we report impedance spectroscopy study of Fe-N-C electrocatalyst integrated into cathodic catalyst layers of PEM fuel cell with various cathode catalyst layer (CCL) configurations. We fit the physics-based impedance model, which takes into account oxygen transport in the cathode catalyst layer, gas diffusion layer (GDL) and flow-field channels to the experimental spectra. The dependencies of the Tafel slope, double layer capacitance, electrode proton conductivity and oxygen diffusivity on the cell current density in the range of 0.025 to 0.4 A cm^{-2} are obtained and compared to the standard Pt/C electrode.

Experimental

Catalyst preparation.—The PGM-free catalyst studied in the present work was synthesized by modified Sacrificial Support Method (SSM).[14,15] The catalyst entitled as Fe-NMCU was prepared by mixing the 2.5 g of iron (III) nitrate ($Fe(NO_3)_3$*$9H_2O$, Sigma-Aldrich) with 15 g of nicarbazin (NCB, Sigma-Aldrich), 10 g of mebendazole (MBZ), 5 g of carbendazim (CBDZ, Sigma-Aldrich) and 5 g of urea (UR, Sigma-Aldrich) in 500 mL of water. The slurry of organic precursors and iron nitrate was heated to T = 75°C under magnetic stirring and 10 g of LM150 fumed silica (Cabot, surface area ~ 150 m^2 g^{-1}) was added in 1 g increments to ensure homogeneous mixing. The water was allowed to evaporate, and solid powder was pyrolyzed for 45 min at 975°C in the flow of ultra-high purity (UHP) nitrogen, 100 ccm. After the heat treatment, silica was etched away by 40 wt% HF, followed by washing with DI water until neutral pH was obtained (pH ~ 6.7). The prepared powder was then dried overnight in an oven at T = 85°C. Second heat treatment was performed in a reactive atmosphere of 20 at% NH_3 at a flow rate of 100 ccm to remove unwashed H_2SiF_6. This second heat treatment was performed for 30 min at 975°C.

*Electrochemical Society Member.
zE-mail: A.Kulikovsky@fz-juelich.de

Table I. The main structural parameters of the cathodes and PEMFC operating conditions.

Parameters	MEA1	MEA2	MEA3	MEA4
Catalyst loading, mg cm^{-2}	3.0	3.0	1.5	1.5
Nafion loading, wt%	35	45	35	45
Catalyst layer thickness l_t, μm	130	140	70	70
Gas diffusion layer thickness l_b, μm	235			
Relative humidity (RH), %	100			
Cathode absolute pressure, kPa	304			
Cell temperature, K	273 + 80			

Ink fabrication and spraying.—Catalyst ink were prepared by mixing the catalyst powder with the ionomer (Nafion, EW = 1100, Fuel Cell Store), water and Isopropyl Alcohol (IPA). The inks were mixed at different ratio of catalyst to ionomer: 35 wt% and 45 wt% as well as two different loadings of PGM-free catalyst on the GDL: 1.5 and 3 mg cm^{-2}. The mixture of catalysts powder IPA, water and ionomer, were loaded in the agate ball mill jar. Then the jar was kept centrifuging for 1 hr to make homogeneous inks. After preparation, cathode inks were sprayed using spray gun on the GDL (SGL, 29BC). Sprayed area was 7.6 cm^2 (16 × 47.5 mm^2). The temperature of GDL was maintained at 50–55°C while spraying to prevent cracking the catalyst layer. For MEA preparation we used a segmented gasket and 10 hand-sprayed cathode gas diffusion electrodes (GDEs, 7.6 cm^2), whereas the anode utilized a single GDE from Alfa Aesar (100 cm^2, 0.1 mg$_{Pt}$ cm^{-2}). The gaskets were made of Teflon, and the anode and cathode were 125 μm thick. The MEAs were assembled by hot pressing the gaskets, the Alfa Aesar anode GDE, membrane (Nafion XL, 25 μm) and the ten hand-sprayed cathodes GDEs at 135°C and 5000 pounds force for 5 minutes. The samples details are presented at Table I.

Electrochemical studies.—Electrochemical evaluation has been performed using a segmented cell system and a test station developed at Hawaii Natural Energy Institute (HNEI). The segmented cell setup consists of a cell hardware, a custom designed current transducer system, a data acquisition device and a single cell test station. The transducer system utilizes closed loop Hall sensors (Honeywell CSNN 191) for current detection and can operate in a high current (up to 15 A) and a low current (up to 0.375 A) mode. Data collection is performed with a National Instrument PXI data acquisition instrument operating under HNEI-developed control and acquisition LabView programs. The configuration of the segmented cell setup allows the system to simultaneously record localized current-voltage response as well as EIS and cyclic voltammetry (CV) data. Further details of the segmented cell system can be found in Ref. 16.

The segmented cell hardware is based on an HNEI 100 cm^2 cell design and consists of non-segmented and segmented flow field plates. Both flow field plates have the same ten parallel channel serpentine design and arranged in co-flow configuration. The segmented flow field plate consists of 10 electrically insulated segments with an area of 7.6 cm^2 and connected in consequent order form inlet (segment 1) to outlet (segment 10). In our experimental fuel cell design, the segmentation was applied to the cathode.

The polarization curves (VI curves) were measured under galvanostatic control of the total cell current at the cell temperature of 80°C. The anode/cathode testing conditions were a 2/2 stoichiometric ratio of H_2/air (or O_2), 100/100% relative humidity and 304 kPa backpressure. To maintain constant water transport in the cell at any given total cell current density, the flow rates of H_2/O_2 were identical to those used during the H_2/air experiments at stoichiometry of 2/2. Consequently, the stoichiometry of O_2 increased to 9.5. The resulting two different VI curves (H_2/air and H_2/O_2) were used for the determination of electrodes activation, ohmic and mass transfer overpotentials as described in Refs. 16, 17. In order to understand mass transport phenomena and for modelling purposes additional IV curves were recorded at H_2/air gas configuration with 2/9.5 stoichiometry. The VI curve measurements were combined with EIS to determine the high-frequency resistances (HFR) and collect the electrochemical impedance spectra for all ten segments and the overall cell. The selected frequency range for the EIS experiments was 0.05 Hz to 10 kHz and the amplitude of sinusoidal current signal corresponded to a cell voltage perturbation of 10 mV or lower. The HFR was determined from the intercept of the EIS with the real axis at higher frequencies at the Nyquist plot.

Scanning Electron Microscopy (SEM) images of the Membrane Electrode Assemblies (MEAs) cross-sections were obtained with a Hitachi S-4800 field emission microscope with accelerating voltage of 5 kV.

Impedance Model

Basic equations.—Details of the impedance model used in the present work have been reported in Refs. 18, 19. Here, we briefly discuss the basic model equations. It is supposed that the cell active area is separated into N equal segments. The core of the model is a system of transient equations for the conservation of charge and oxygen mass in the CCL of an individual segment:

$$C_{dl}\frac{\partial \eta}{\partial t}+\frac{\partial j}{\partial x}=-i_*\left(\frac{c}{c_h}\right)\exp\left(\frac{\eta}{b}\right) \quad [1]$$

$$j=-\sigma_0 s\,(x)\,\frac{\partial \eta}{\partial x} \quad [2]$$

$$\frac{\partial c}{\partial t}-D_{ox}\frac{\partial^2 c}{\partial x^2}=-\frac{i_*}{4F}\left(\frac{c}{c_h^{in}}\right)\exp\left(\frac{\eta}{b}\right) \quad [3]$$

Here, C_{dl} is the double layer volumetric capacitance (per unit electrode volume, F cm^{-3}), η is the positive by convention ORR overpotential, t is time, j is the local proton current density, x is the distance from the membrane through the electrode depth, i_* is the volumetric exchange current density (A cm^{-3}), c is the local oxygen concentration, c_h^{in} is its reference concentration, b is the ORR Tafel slope per exponential basis, σ_o is the CCL proton conductivity at the membrane/CCL interface, $s(x)$ is the conductivity shaping function, and D_{ox} is the effective oxygen diffusion coefficient in the CCL.

Eq. 1 is the proton charge conservation, Eq. 2 is the Ohm's law relating the proton current density to the gradient of overpotential, and Eq. 3 is the oxygen mass balance equation with the Fick's law of diffusion. The CCL proton conductivity is assumed to be a function of the coordinate through the CCL depth $\sigma_p = \sigma_o\, s(x)$ with the shape function $s(x)$ given by

$$s=\exp\left(-\beta\frac{x}{l_t}\right) \quad [4]$$

Here, β is the inverse characteristic scale of the exponent and l_t is the CCL thickness. The exponential decay of σ_p with x provides a reasonably good fit of the high-frequency (HF) part of the spectra. With $\beta = 0$ (uniform σ_p), the model gives a 45°- straight line in the HF part of the Nyquist spectrum, which is a signature of proton transport in a uniform catalyst layer.[20] However, it should be mentioned that all experimentally evaluated electrodes exhibit the slope of the spectrum exceeding 45° in the high-frequency domain. In Ref. 13, this effect has been attributed to non-uniform filling of CCL micro-pores with Nafion, leading to variable shape of the pore volume. Another explanation is a non-uniform σ_p shape through the CCL depth;[21–24] here, we adopt the last conjecture and set $\beta = 3$ for all the studied electrodes. Variation of σ_p with x could be either due to higher fraction of Nafion in the electrode close to the membrane, or due to higher rate of liquid water production at the CCL/membrane interface. Detailed discussion of Eqs. 1–3 is given in Ref. 18.

The oxygen mass transport in the GDL is also described by the Fick's type diffusion equation

$$\frac{\partial c_b}{\partial t} - D_b \frac{\partial^2 c_b}{\partial x^2} = 0 \quad [5]$$

where c_b is the oxygen concentration and D_b is the oxygen diffusion coefficient in the GDL. The segment problems are "linked" by the oxygen mass transport in the channel:

$$\frac{\partial c_h}{\partial t} + v\frac{\partial c_h}{\partial z} = -\frac{N_b}{h} \quad [6]$$

where c_h is the oxygen concentration in the channel, v is the flow velocity (assumed to be constant), z is the distance along the channel counted from the inlet, h is the channel depth, and

$$N_b = D_b \frac{\partial c_b}{\partial x}\bigg|_{x=l_t+l_b} \quad [7]$$

is the oxygen flux in the GDL at the CDL/channel interface. Here, l_b is the GDL thickness. Solution to Eq. 6 provides a boundary condition for the local segment problems. Note that in this work we assume that the CCL and the GDL transport parameters are the same in all segments, i.e., we do not take into account possible effects of local cell flooding. Under this assumption, the model gives the average over the cell surface parameters (see below).

The system of Equations 1–7 is completed with the boundary and interface conditions, which express continuity of the oxygen concentration and flux at the channel/GDL and GDL/CCL interfaces, zero proton current at the GDL/CCL interface, and zero oxygen flux at the membrane interface.[19]

Numerical details.—Equations 1–6 have been linearized and Fourier-transformed to yield a system of linear equations for the perturbation amplitudes of overpotential η^1 and oxygen concentrations c^1 c_b^1 and c_h^1. Here, the superscript 1 marks small-amplitude perturbations. The code for fitting experimental spectra has been developed in Python environment. The boundary-value problems for the perturbation amplitudes and for the static shapes of overpotential and oxygen concentrations have been solved using the SciPy library subroutine *solve_bvp*. The Cauchy problem for the linearized version of Eq. 6 has been solved using the *odeint* solver from SciPy library. The fitting itself has been performed by invoking the *least squares* module from the SciPy. To accelerate calculations, a parallel version of the code has been developed using the *mpi4py* library for Python. The code effectively loads multi-core processors of modern PCs providing three- to four-fold acceleration of calculations on a PC with the quad-core processor. The CCL parameters used in the calculations are listed in Table I.

Results and Discussion

Polarization curves.—Scanning electrone microscopy was used to visualize electrode homogeniety on the macroscopic level (tens of micrometers) and to estimate the electrode thickenss in dependence of catalyst loading and ionomer content. A representative SEM pictures of the MEA1 and MEA3 cathodes are shown at Fig. 1. The SEM images have been used to evaluate the thicknesses of the CCL, GDL and membrane. According to calculation of the PGM-free catalyst layer (CL) thicknesses the main factor which affects these values is catalyst loading. The independence of CL thickness from ionomer content may indicate the preferential distribution of Nafion inside of large pores of Fe-N-C catalyst synthesized by Sacrificial Support Method.[25] The cathode thickness was found to be 120–140 μm for a sample with 3.0 mg cm^{-2} catalyst loading (Fig. 1a), while a catalyst content to 1.5 mg cm^{-2} caused appropriate decrease in the thickness to 70 μm (Fig. 1b). Membrane thickness was found to be 30±5 μm.

Polarization curves and HFR recorded for overall cell under galvanostatic control of load and at H_2/air and H_2/O_2 operating conditions are presented at Figs. 2a and 2b, respectively. Operation with air as an oxidant resulted in lower performance compared to oxygen. Interestingly, MEA2 clearly showed a drop of the performance at current densities higher than 0.2 A cm^{-2} most likely due to mass transfer limitation of the PGM-free electrode formulation (Fig. 2a). Moreover, the spatial performance of inlet segments 1–5 was not affected, while segments 6–10 demonstrated a rapid voltage loss from 0.6 to 0.35 V. On the contrary, performance of MEA2 significantly improved when stoichiometry of air was increased from 2 to 9.5 or by changing air to oxygen (Figs. 2b, 2c). At the conditions of high oxidant flow MEA2 showed the best performance compared to others. HFR of the samples was found to be quite uniform and varied in the range of 0.08–0.1 Ω cm^2. The obtained H_2/O_2 and H_2/air IV curves were used to determine activation and mass transfer overpotentials as described in our previous works[16,17] (Fig. 2d). PGM-free systems are characterized by high activation losses compared to Pt/C, for example, 570–625 mV vs 340 mV at 0.1 A cm^{-2} for PGM-free and standard-Pt cathode electrode (0.4 mg$_{Pt}$ cm^{-2}), respectively.[16,17] Mass transfer losses were found to increase with operating current as well as with PGM-free catalyst loading. MEA1 is characterized by the greatest mass transfer overpotential at 0.3 A cm^{-2} compared to other samples, while MEA2 demonstrated high mass transfer limitations even at low current. Thus, two samples with 3.0 mg cm^{-2} catalyst loading have significant mass transfer losses. It should be also mentioned that mass transfer losses for PGM-free fuel cells were higher than in the case of Pt/C due to the catalyst loading and electrode thickness: 70–140 μm for Fe-N-C and 10–12 μm for 0.4 mg$_{Pt}$ cm^{-2} Pt/C electrode.[26] The mass transfer overpotential was determined to be 160–230 mV and ∼60 mV at 0.8 A cm^{-2} for PGM-free samples and standard Pt/C cathode, respectively. Analysis of H_2/O_2 polarization curves revealed that the Tafel slope of PGM-free systems varies in the range of 164–190 mV/dec which is almost twice higher as compared to Pt/C. The distribution of Tafel slope values over the active area of MEA is uniform and does not depend on the location (Fig. 2e).

Impedance spectra.—An example of the experimental and fitted model spectra is shown in Fig. 3. As can be seen, the quality of spectra fitting is good for a high air stoichiometry λ (Fig. 3a), and it lowers with

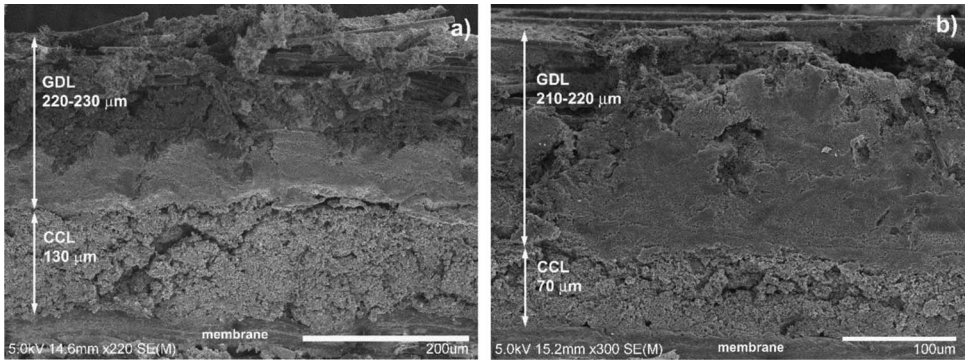

Figure 1. SEM images of the cathode electrodes: (a) – MEA1 (3 mg cm^{-2}, 35wt% Nafion); (b) – MEA3 (1.5 mg cm^{-2}, 35wt% Nafion).

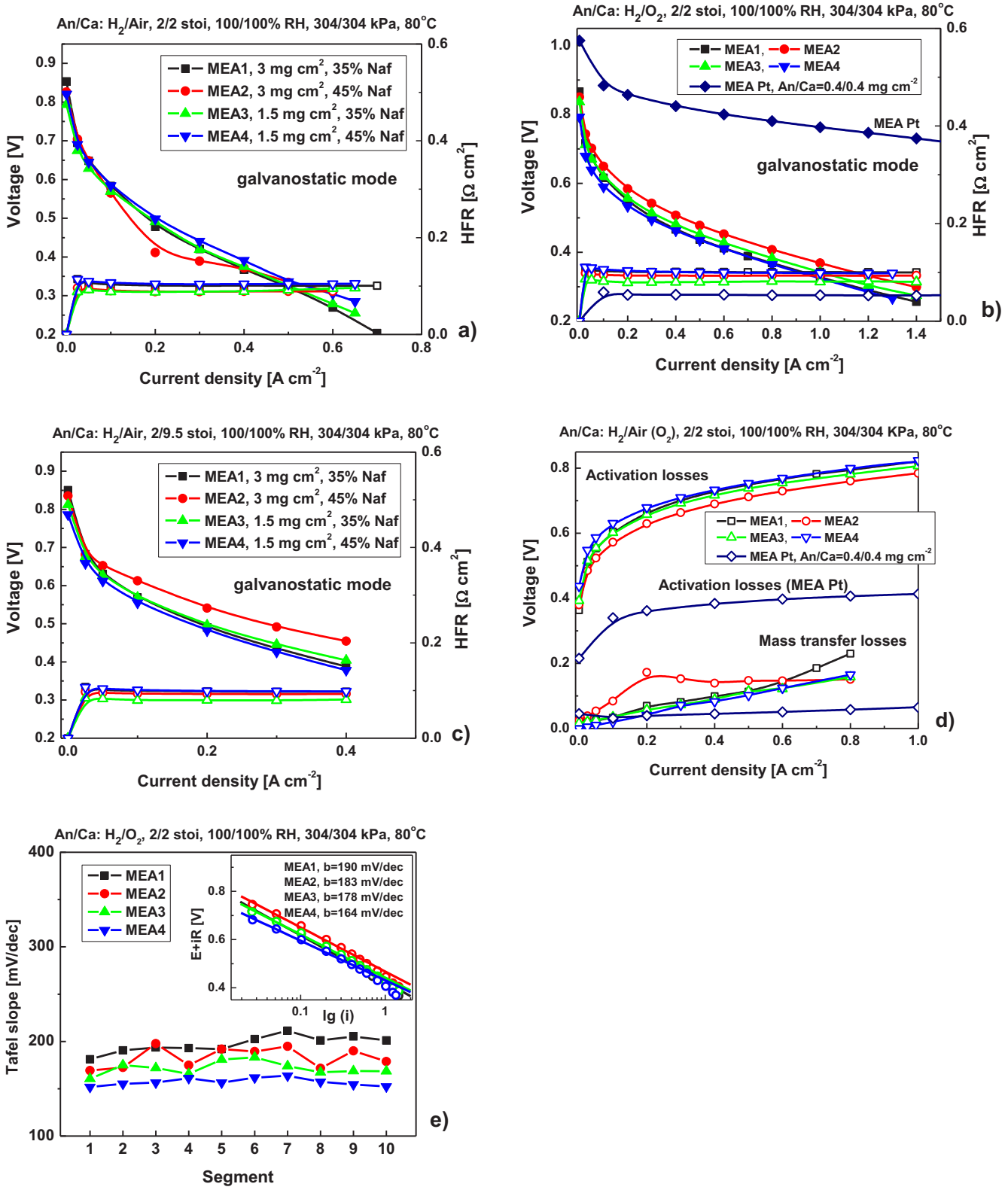

Figure 2. Polarization curves recorded of the tested cells using air as a cathode feed gas (a, b) and oxygen (c). Activation and mass transfer losses as function of current density (d). Distributions of Tafel slope values vs segment location (e). Anode/cathode: H_2/air (O_2), 2/2 (9.5) stoichiometry, 100/100% RH, 304/304 kPa, 80°C. For Pt MEA Anode/cathode: H_2/O_2, 2/9.5 stoichiometry, 100/50% RH, 150/150 kPa, 80°C.

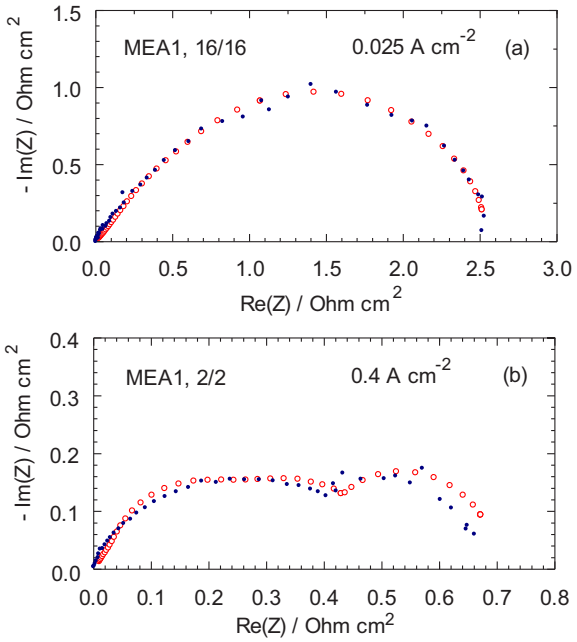

Figure 3. Experimental (filled points) and fitted model (open symbols) spectra of the PEM fuel cell with the MEA1 and air stoichiometry of 16 for the current density of (a) 0.025 A cm^{-2} and (b) $\lambda = 2$ for 0.4 A cm^{-2}. The experimental and fitted points are shown for the same frequencies *f*.

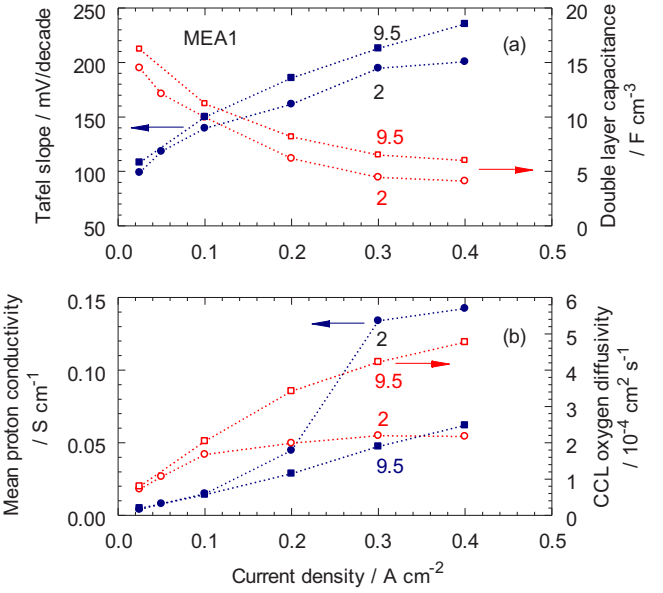

Figure 5. The dependence of cell transport and kinetic parameters on the cell current density. Shown are the results for MEA1 running with air stoichiometry of 2 and 9.5. (a) The Tafel slope (blue lines) and the double layer capacitance (red lines), (b) the CCL proton conductivity (blue lines) and oxygen diffusivity (red lines).

the decrease of λ (Fig. 3b). Lower quality of spectra fitting at $\lambda = 2$ and higher current density is most probable due to non-uniform distribution of one or several transport parameters over the cell surface area. Bode plots of Im (*Z*) vs frequency for the same spectra are depicted in Fig. 4. As can be seen, the model does not fit well the two to three most low-frequency points; perhaps, due to effect of slow dynamic of adsorbates on the catalyst surface, which is ignored in the model.

Figs. 5–8 show the resulting from fitting dependence of MEA transport and kinetic parameters on the cell current density. In all the tested electrodes, the ORR Tafel slope *b* increases with the cell current from 100 mV/dec at 0.025 A cm^{-2}, to 250 mV/dec at 0.4 A cm^{-2} (Figs. 5a–8a); these values are in good agreement with those obtained from IV curves (Fig. 2d) Wide range of *b* variation is a largest limitation of the tested electrodes; in the standard Pt/C-based systems this parameter varies from 70 to 90 mV/dec in the same range of cell currents.[27] Note that the model above takes into account the effect of apparent Tafel slope doubling due to poor proton and/or oxygen transport in the CCL; Figs. 5a–8a thus show the intrinsic kinetic value of this parameter. Recent microstructural studies indicate several types of the Fe-N-C sites, where the ORR takes place.[9–11] The physics of strong *b* variation could be attributed to the change of a preferential for ORR type of the Fe-N-C site as the electrode potential decreases. Higher Tafel slopes indicate hindrances in charge transfer (low turn-over frequency per site).

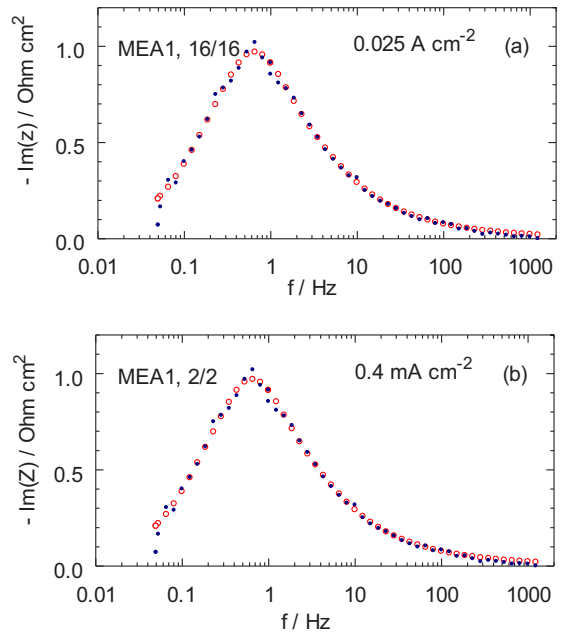

Figure 4. Bode plots of Im (*Z*) vs frequency for the spectra in Fig. 3.

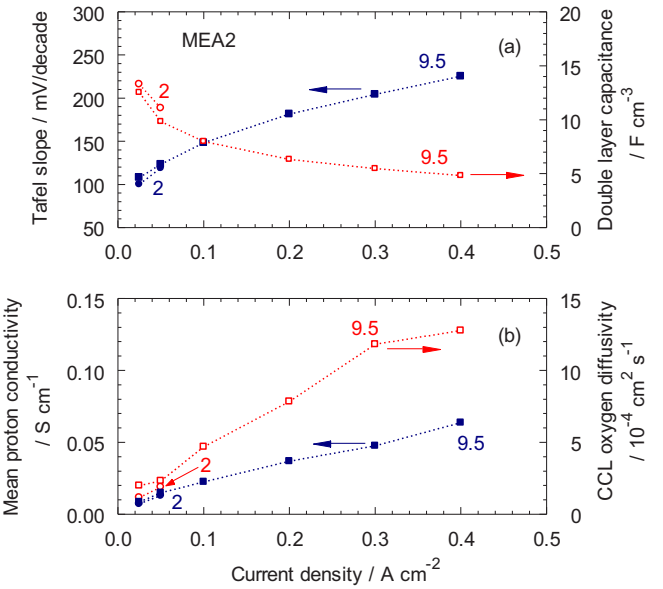

Figure 6. The same as in Figure 5 for the MEA2.

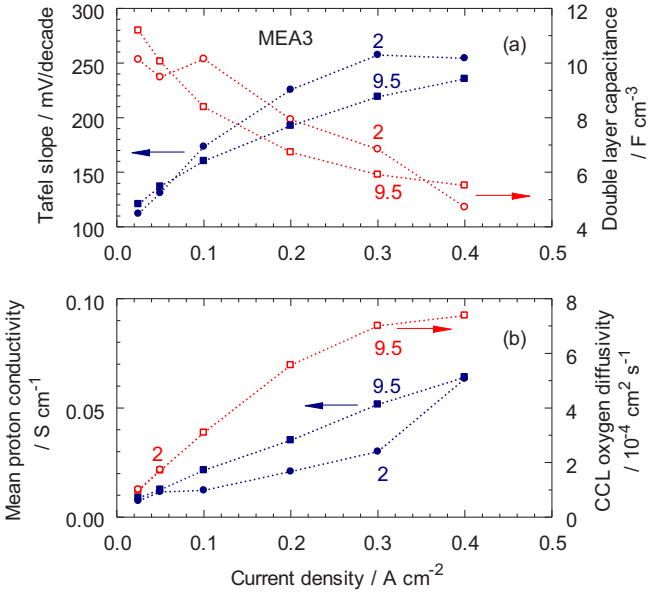

Figure 7. The same as in Fig. 5 for the MEA3.

The double layer capacitance decreases from 10 F cm^{-3} at 0.025 A cm^{-2} to 4–6 F cm^{-3} at 0.4 A cm^{-2} in the electrodes MEA1, MEA2 and MEA3, and from 20–25 F cm^{-3} to 10 F cm^{-3} in MEA4 (Figs. 5a–8a). Lowering of C_{dl} is seemingly due to accumulation of liquid water in the electrodes with the increase of J. Note that in Pt/C electrode, C_{dl} also lowers with J; however, from 20–30 F cm^{-3} to ≈ 10 F cm^{-3}.[27] Twice lower C_{dl} in the Fe-N-C systems MEA1, MEA2 and MEA3 can be attributed to the difference in the morphology of Pt/C and PGM-free catalysts. In the case of relatively large carbon structures decorated with platinum nanoparticles water film can be effectively removed due to the hydrophobic properties of carbon and gradient of humidity in GDL. The studied Fe-N-C catalyst possesses highly developed internal porous structure, which is populated with Fe-N$_x$ active sites. Despite the highly hydrophobic bulk properties of these Fe-N-C catalyst the flooding effect can be irreversible and once flooded micropores (≤1 nm) cannot expel water at fuel cell conditions selected in the present work. As it was reported recently, the durability issues

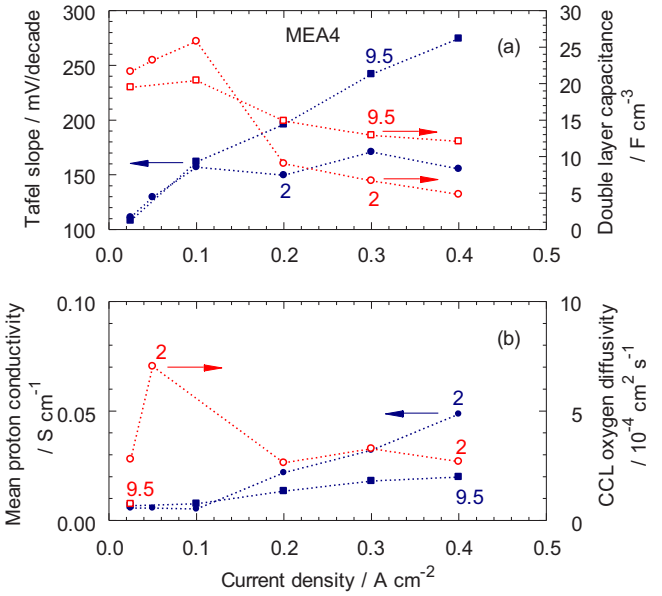

Figure 8. The same as in Fig. 5 for the MEA4.

of metal-organic framework (MOF) derived PGM-free materials as well as pre-commercial M-N-C catalysts were not correlated to the flooding of the cathode, which can be indication of intrinsic differences of SSM-derived catalysts.[28,29]

The mean through the CCL depth proton conductivity increases with the cell current from 0.005 S cm^{-1} to about 0.07 S cm^{-1} in the range of cell currents 0.025 to 0.4 A cm^{-2} (Figs. 5b–8b). The growth of σ_p with J could partly be explained by increasing amount of liquid water in the CCL. On the other hand, Modestov et al.[30] reported a seven- to twenty-fold increase in the CCL conductivity when the electrode potential decreased from 1 to 0.1 V. They attributed this growth to ionization of surface acidic groups on carbon support, which leads to increasing proton concentration in an electrode at low cell potentials.

The last parameter returned by the model is the CCL oxygen diffusivity D_{ox}. In all the tested electrodes D_{ox} is very large in spite on their significant thickness (Figs. 5b–8b). Like in Pt/C systems, D_{ox} increases with the cell current by a factor of ten; here, however, D_{ox} is nearly an order of magnitude higher, than in the standard Pt/C electrodes (0.5–2.5·10^{-4} cm^2 s^{-1}).[26] D_{ox} varies from ≈10^{-4} cm^2 s^{-1} at 0.025 A cm^{-2} to nearly 10^{-3} cm^2 s^{-1} at 0.4 A cm^{-2} (Figs. 5b, 6b, 7b). The only exception is the MEA4 electrode, in which D_{ox} does not grow with the cell current, staying on the level of ≈ 3·10^{-4} cm^2 s^{-1} (Fig. 8b). The same trend of increasing D_{ox} (J) (though in the lower range of absolute values) has been found in the Pt/C cathode; the physics of D_{ox} growth with J requires additional studies. All these findings are in good correlation with expected oxygen diffusivity through the extremely porous 3D structure of this class of Fe-N-C ORR catalyst.

In all the variants, the model was not able to capture the GDL oxygen diffusivity. This means that either the respective impedance values are small, and they cannot be determined by the fitting procedure, or the characteristic frequencies of oxygen transport in the CCL and the GDL are close to each other, making these processes indistinguishable by impedance spectroscopy.

The results above allow us to estimate two key performance parameters of the electrodes: the characteristic current densities for proton j_p and oxygen j_{ox} transport

$$j_p = \frac{\sigma_p b}{l_t}, \quad j_{ox} = \frac{4F D_{ox} c_1}{l_t} \qquad [8]$$

where c_1 is the oxygen concentration at the CCL/GDL interface, σ_p is the mean through the CCL depth proton conductivity. Note that in all equations of this work, b is given per exponential basis, i.e., the data in Figs. 5a, 6a, 7a and 8a must be divided by 2.303 for using in Eq. 8.

If the mean current density $J > j_p$, the ORR peak forms at the membrane/CCL interface, where the protons are "cheaper". If $J > j_{ox}$, the reaction shifts to the CCL/GDL interface, where oxygen is readily available. In both cases, large fraction of the electrode thickness does not participate in the reaction and the apparent Tafel slope doubles due to transport problems.[31,32] In a well-designed electrode, the following relations should hold:

$$J \leq j_p \simeq j_{ox} \qquad [9]$$

Note that in Pt/C systems, $b \approx 0.03$ V is weakly dependent on J, while D_{ox} increases with J from ≈ 10^{-5} cm^2 s^{-1} at 0.025 A cm^{-2}, to about 10^{-4} cm^2 s^{-1} at 0.025 A cm^{-2} at 0.4 A cm^{-2}.[26]

All the tested electrodes exhibit quite strong variation of parameters appearing in Eq. 8 with the current density; it is, thus, advisable to plot the dependencies $j_p(J)$ and $j_{ox}(J)$ (Fig. 9). For the upper estimate of j_{ox}, we neglect oxygen transport loss in the GDL and set $c_1 = c_h^{in}$.

As can be seen, the best-performing electrodes are MEA2 and MEA3 at the air stoichiometry of 9.5 (Figs. 9d, 9f). Note that MEA 3 has low catalyst loading and Nafion of 35 wt.%, while MEA 2 has high catalyst and Nafion contents. Interestingly, the thickest electrode MEA1 exhibits good oxygen transport properties, which can be explained by relatively low blockage of oxygen diffusivity by Nafion film (35wt% vs 45wt% in the case of MEA2) (Figs. 9a, 9b), while MEA4 demonstrates poor proton transport capabilities (Figs. 9g, 9h) in spite of 45wt% of Nafion loading. Moreover, the ratio of J to j_p increases

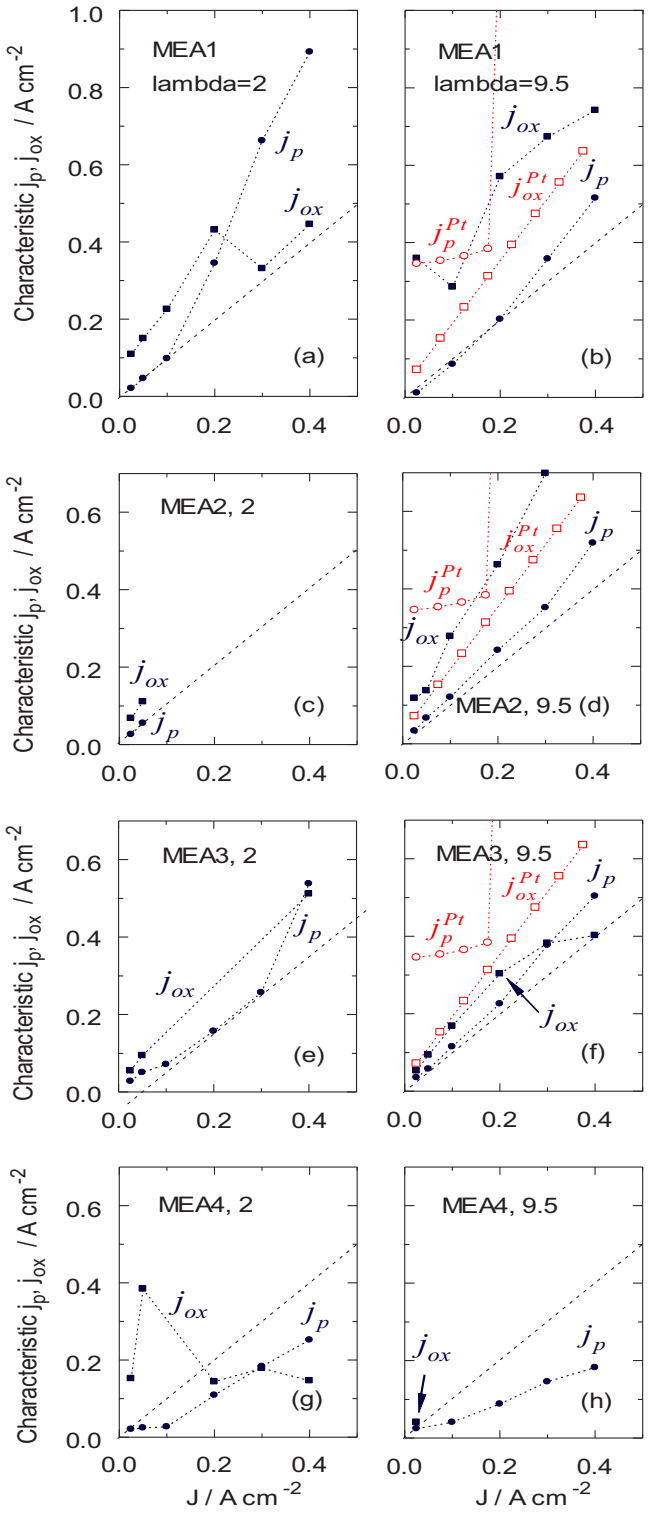

Figure 9. Characteristic current densities for proton j_p (filled circles) and oxygen j_{ox} (filled squares) transport in the electrodes MEA1, MEA2, MEA3 and MEA4 for the air flow stoichiometry 2 (left column) and 9.5 (right column) as a function of the mean cell current density J. Dashed 45°-line corresponds to $j_p = j_{ox} = J$. For comparison, j_p and j_{ox} for a standard Pt/C electrode[27] are shown (open symbols).

with the cell current, reaching a factor of two at $J = 0.4$ A cm^{-2} for MEA4 (Fig. 9h). In addition, j_{ox} in this electrode is independent of J, and at $J = 0.4$ A cm^{-2} it is also twice less than J (Fig. 9g).

For comparison, the curves $j_p^{Pt}(J)$ and $j_{Ox}^{Pt}(J)$ for the standard Pt/C electrode with Pt loading of 0.4 mg cm^{-2} are shown in Figs. 9b, 9d and 9f.[27] As can be seen, below 0.3 A cm^{-2}, MEA2 and MEA3 do not lose much to the Pt/C system. Note, however, that the absolute value of the Tafel slope in all the tested electrodes is much larger, than in the Pt/C cathode. At the cell current of 0.4 A cm^{-2}, even the best-performing electrodes MEA2 and MEA3 exhibit $b \approx 250$ mV/dec, while in the Pt/C electrode $b \approx 100$ mV/dec.[27] This means, that the ORR kinetic losses in the Fe-N-C systems are much higher, than in the Pt/C.

An analysis of different CCL configurations shows that j_p and j_{ox} strongly depend on catalyst and Nafion loadings. Moreover, each catalyst loading value requires its own optimum ionomer content in CCL. The excessive Nafion loading of 45 wt% for low loading PGM-free electrodes most likely caused non-uniform distribution of ionomer through the electrode structure, blocked catalyst centers and resulted in poor proton and oxygen conductivity. While 35 wt% of ionomer was found to be proper to insure sufficient proton and O_2 transport through the electrode with 1.5 mg cm^{-2} of the catalyst. The high PGM-free catalyst loading in CCL needed larger ionomer content to provide the proper transport properties. However, thick catalyst layer with good proton conductivity is prone to flooding at low air stoichiometry, when produced water cannot be removed efficiently. Only high air stoichiometry or pure oxygen operation could ensure sufficient water transport and good performance. On the other hand, the flooding issue at low air flows could be avoided by tailored design of CCL textural properties insuring not only O_2 but also water transport.

Conclusions

We report impedance spectroscopy study of four PEM fuel cells equipped with the Fe-N-C-based cathodes with varied catalyst and ionomer loadings. A recent physics-based model for PEMFC impedance is fitted to the experimental spectra and the dependence of kinetic and transport parameters on the mean cell current density J in the range from 0.025 to 0.4 A cm^{-2} are obtained. A summary of the results is as following.

- The double layer capacitance of all the electrodes decreases from 10–15 F cm^{-3} at 0.025 A cm^{-2} to ≈ 5 F cm^{-3} at 0.4 A cm^{-2}. This decay could be attributed to accumulation of liquid water in the electrode. This could also be due to a selectivity change and engaging of the ORR alternative N-containing moieties in a dual-site mechanism.[9]
- The CCL mean proton conductivity σ_p and oxygen diffusivity D_{ox} increase with the cell current density by a factor of ten. Both effects take place also in Pt/C systems;[27] however, the absolute value of D_{ox} in the Fe-N-C electrodes is an order of magnitude higher, than in the Pt/C cathodes. The growth of σ_p with J partly is due to accumulation of liquid water in the CCL; however, it may also be due to ionization of acidic molecules on carbon surface at lower cell potentials, as suggested in Ref. 30.
- In the range of cell currents discussed, the Tafel slope of all the electrodes varies from 100 to 250 mV/dec. For comparison, in the Pt/C electrode this parameter varies from 70 to 100 mV/dec in the same range of currents.
- Calculation of the characteristic current densities for proton j_p and oxygen j_{ox} transport in the CCL shows that MEA1, MEA2 and MEA3 are well-balanced, i.e., j_p and j_{ox} in these electrodes exceed J. This means, that the polarization curves of these systems do not exhibit doubling of apparent Tafel slope due to transport problems. However, in MEA4 $j_p < J$ in the whole range of J, meaning that the apparent Tafel slope increases with J due to poor proton transport.
- The largest problem of all the electrodes is high absolute value of the kinetic Tafel slope. This parameter is responsible for faster decay of the cell polarization curve as compared to Pt/C-based PEMFCs.

Acknowledgments

T. Reshetenko gratefully acknowledges funding from US Office of Naval Research (N00014-18-1-2127). This work was supported by US DOE EERE grant DE-EE0008419 "Active and Durable PGM-free Cathodic Electrocatalysts for Fuel Cell Application" PI: Alexey Serov. The authors are thankful to Rohan Gokhale for preparing some electrode samples, Tina Carvalho for assisting with SEM, Günter Randolf and Jack Huizingh for valuable help in the system operation and the Hawaiian Electric Company for ongoing support of the Hawaii Sustainable Energy Research Facility.

ORCID

Tatyana Reshetenko https://orcid.org/0000-0002-4552-062X
Andrei Kulikovsky https://orcid.org/0000-0003-1319-576X

References

1. Prof. Schoenbein, "On the voltaic polarization of certain solid and fluid substances." *Phil. Mag.*, **XIV**, 43 (1839).
2. S. T. Thompson, A. R. Wilson, P. Zelenay, D. J. Myers, K. L. More, K. C. Neyerlin, and D. Papageorgopoulos, "ElectroCat: DOE's approach to PGM-free catalyst and electrode R&D." *Solid State Ionics*, **319**, 68 (2018).
3. U. Martinez, S. K. Babu, E. F. Holby, and P. Zelenay, "Durability challenges and perspective in the development of PGM-free electrocatalysts for the oxygen reduction reaction." *Current Opinion Electrochem.*, **9**, 224 (2018).
4. A. Serov, K. Artyushkova, E. Niangar, C. Wang, N. Dale, F. Jaouen, M.-T. Sougrati, Q. Jia, S. Mukerjee, and P. Atanassov, "Nano-structured non-platinum catalysts for automotive fuel cell application." *Nano Energy*, **16**, 293 (2015).
5. U. Tylus, Q. Jia, K. Strickland, N. Ramaswamy, A. Serov, P. Atanassov, and S. Mukerjee, "Elucidating oxygen reduction active sites in pyrolyzed metal-nitrogen coordinated non-precious metal electrocatalyst systems." *J. Phys. Chem. C*, **118**, 8999 (2014).
6. Q. Jia, N. Ramaswamy, U. Tylus, K. Strickland, J. Li, A. Serov, K. Artyushkova, P. Atanassov, J. Anibal, C. Gumeci, S. C. Barton, M.-T. Sougrati, F. Jaouen, B. Halevi, and S. Mukerjee, "Spectroscopic insights into the nature of active sites in iron-nitrogen-carbon electrocatalysts for oxygen reduction in acid." *Nano Energy*, **29**, 65 (2016).
7. T. Lopes, A. Kucernak, D. Malko, and E. A. Ticianelli, "Mechanistic insights into the oxygen reduction reaction on metal-N-C electrocatalysts under fuel cell conditions." *ChemElectroChem*, **3**, 1 (2016).
8. M. H. Robson, A. Serov, K. Artyushkova, and P. Atanassov, "A mechanistic study of 4-aminoantipyrine and iron derived non-platinum group metal catalyst on the oxygen reduction reaction." *Electrochimica Acta*, **90**, 656 (2013).
9. Y. Chen, I. Matanovic, E. Weiler, P. Atanassov, and K. Artyushkova, "Mechanism of oxygen reduction reaction on transition metal-nitrogen-carbon catalysts: Establishing the role of nitrogen-containing active sites." *ACS Appl. Energy Mater.*, **1**, 5948 (2018).
10. I. Matanovic, K. Artyushkova, and P. Atanassov, "Understanding PGM-free catalysts by linking density functional theory calculations and structural analysis: Perspectives and challenges." *Current Opinion in Electrochem.*, **9**, 137 (2018).
11. J. Li and F. Jaouen, "Structure and activity of metal-centered coordination sites in pyrolyzed metal-nitrogen-carbon catalysts for the electrochemical reduction of O_2." *Current Opinion in Electrochem.*, **9**, 198 (2018).
12. S. Stariha, K. Artyushkova, M. J. Workman, A. Serov, S. Mckinney, B. Halevi, and P. Atanassov, "PGM free Fe-N-C catalysts for oxygen reduction reaction: Catalyst layer design." *J. Power Sources*, **326**, 43 (2016).
13. D. Malko, T. Lopes, E. A. Ticianelli, and A. Kucernak, "A catalyst layer optimization approach using electrochemical impedance spectroscopy for PEM fuel cells operated with pyrolysed transition metal-N-C catalysts." *J. Power Sources*, **323**, 189 (2016).
14. D. Sebastian, A. Serov, K. Artyushkova, P. Atanassov, A. S. Arico, and V. Baglio, "Performance, methanol tolerance and stability of Fe{aminobenzimidazole derived catalyst for direct methanol fuel cells." *J. Power Sources*, **319**, 235 (2016).
15. D. Sebastian, A. Serov, I. Matanovic, K. Artyushkova, P. Atanassov, A. S. Arico, and V. Baglio, "Insights on the extraordinary tolerance to alcohols of Fe-N-C cathode catalysts in highly performing direct alcohol fuel cells." *Nano Energy*, **34**, 195 (2017).
16. T. V. Reshetenko, G. Bender, K. Bethune, and R. Rocheleau, "Systematic study of back pressure and anode stoichiometry effects on spatial PEMFC performance distribution." *Electrochimica Acta*, **56**, 8700 (2011).
17. T. V. Reshetenko, A. Serov, K. Artyushkova, I. Matanovic, S. Stariha, and P. Atanassov, "Tolerance of non-platinum group metals cathodes proton exchange membrane fuel cells to air contaminants." *J. Power Sources*, **324**, 556 (2016).
18. A. A. Kulikovsky, "A physical model for the catalyst layer impedance." *J. Electroanal. Chem.*, **669**, 28 (2012).
19. A. Kulikovsky and O. Shamardina, "A model for PEM fuel cell impedance: Oxygen ow in the channel triggers spatial and frequency oscillations of the local impedance." *J. Electrochem. Soc.*, **162**, F1068 (2015).
20. M. Eikerling and A. A. Kornyshev, "Electrochemical impedance of the cathode catalyst layer in polymer electrolyte fuel cells." *J. Electroanal. Chem.*, **475**, 107 (1999).
21. M. C. Lefevre, R. B. Martin, and P. G. Pickup, "Characterization of ionic conductivity profiles within proton exchange membrane fuel cell gas diffusion electrodes by impedance spectroscopy." *Electrochem. Solid State Lett.*, **2**, 259 (1999).
22. G. Li and P. G. Pickup, "Ionic conductivity of PEMFC electrodes. Effect of Nafion loading." *J. Electrochem. Soc.*, **150**, C745 (2003).
23. D. Gerteisen, "Impact of inhomogeneous catalyst layer properties on impedance spectra of polymer electrolyte membrane fuel cells." *J. Electrochem. Soc.*, **162**, F1431 (2015).
24. T. Reshetenko and A. Kulikovsky, "Impedance spectroscopy study of the PEM fuel cell cathode with nonuniform nafion loading." *J. Electrochem. Soc.*, **164**, E3016 (2017).
25. A. Serov, A. D. Shum, X. Xiao, V. D. Andrade, K. Artyushkova, and I. V. Zenyuk, P. Atanassov "Nano-structured platinum group metal-free catalysts and their integration in fuel cell electrode architectures" *Appl. Catalysis B*, **237**, 1139 (2018).
26. T. Reshetenko and A. Kulikovsky, "Impedance spectroscopy characterization of oxygen transport in low- and high-Pt loaded PEM fuel cells," *J. Electrochem. Soc.*, **164**(14), F1633 (2017).
27. T. Reshetenko and A. Kulikovsky, "Variation of PEM fuel cell physical parameters with current: Impedance spectroscopy study." *J. Electrochem. Soc.*, **163**(9), F1100 (2016).
28. J.-Y. Choi, L. Yang, T. Kishimoto, X. Fu, S. Ye, Z. Chen, and D. Banham, "Is the rapid initial performance loss of Fe/N/C non precious metal catalysts due to micropore flooding?," *Energy Environ. Sci.*, **10**, 296 (2017).
29. D. Banham, T. Kishimoto, Y. Zhou, T. Sato, K. Bai, J. Ozaki, Y. Imashiro, and S. Ye, "Critical advancements in achieving high power and stable nonprecious metal catalyst–based MEAs for real-world proton exchange membrane fuel cell applications," *Sci. Adv.*, **4**, eaar7180 (2018).
30. A. D. Modestov, A. V. Kapustin, V. B. Avakov, I. K. Landgraf, and M. R. Tarasevich, "Cathode catalyst layers with ionomer to carbon mass ratios in the range 0–2 studied by electrochemical impedance spectroscopy, cyclic voltammetry, and performance measurements." *J. Power Sources*, **272**, 735 (2014).
31. M. Eikerling and A. A. Kornyshev, "Modelling the performance of the cathode catalyst layer of polymer electrolyte fuel cells." *J. Electroanal. Chem.*, **453**, 89 (1998).
32. A. A. Kulikovsky, "The regimes of catalyst layer operation in a fuel cell." *Electrochimica Acta*, **55**, 6391 (2010).